Effects of Elevated Extracellular Potassium on the Stimulation Mechanism of Diastolic Cardiac Tissue

Veniamin Y. Sidorov,*† Marcella C. Woods,‡ and John P. Wikswo*†‡§

*Department of Physics and Astronomy; †Vanderbilt Institute for Integrative Biosystems, Research and Education; ‡Department of Biomedical Engineering; and §Department of Molecular Physiology and Biophysics, Vanderbilt University, Nashville, Tennessee

ABSTRACT During cardiac disturbances such as ischemia and hyperkalemia, the extracellular potassium ion concentration is elevated. This in turn changes the resting transmembrane potential and affects the excitability of cardiac tissue. To test the hypothesis that extracellular potassium elevation also alters the stimulation mechanism, we used optical fluorescence imaging to examine the mechanism of diastolic anodal unipolar stimulation of cardiac tissue under 4 mM (normal) and 8 mM (elevated) extracellular potassium. We present several visualization methods that are useful for distinguishing between anodal-make and anodal-break excitation. In the 4-mM situation, stimulation occurred by the make, or stimulus-onset, mechanism that involved propagation out of the virtual cathodes. For 8-mM extracellular potassium, the break or stimulus termination mechanism occurred with propagation out of the virtual anode. We conclude that elevated potassium, as might occur in myocardial ischemia, alters not only stimulation threshold but also the excitation mechanism for anodal stimulation.

INTRODUCTION

The importance of virtual electrode mechanisms in myocardial stimulation using unipolar electrodes has been demonstrated in previous studies (Knisley, 1995; Neunlist and Tung, 1995; Wikswo, Jr. et al., 1995). The bidomain theory revealed that the unequal electrical anisotropies of the intracellular and extracellular spaces play the key role in the virtual electrode appearance (Sepulveda and Wikswo, Jr., 1987; Sepulveda et al., 1989; Wikswo, Jr., 1994; Roth, 1995). During anodal stimulation of myocardium, a dog-bone-shaped region of hyperpolarization oriented transverse to the fiber direction arises centrally around the stimulating electrode. The dog-bone-shaped hyperpolarized region is flanked by two regions of depolarization in the convex portions of the dog-bone.

Virtual electrode stimulation can occur by two mechanisms, known as make-and-break stimulation (Roth, 1995; Wikswo, Jr. et al., 1995). In make-stimulation the excitation originates in the depolarized regions (virtual cathodes) at the onset of the stimulus. Conversely, in break-stimulation the excitation originates in the hyperpolarized region (virtual anode) at the termination of the stimulus pulse. The make-excitation mechanism only occurs when diastolic tissue is stimulated. Break excitation may be induced in both diastolic and systolic tissue by applying a long stimulus or may be induced by means of short stimulus applied during the repolarization phase of the action potential.

In break-stimulation the wave front originates in the virtual anode because of charge diffusion from the virtual cathodes to the virtual anode area (Roth, 1996). The closure of sodium channel inactivation gates due to depolarization leaves the virtual cathode regions unexcitable. However, the sodium channel inactivation gates are open in the hyperpolarized virtual anode region, causing the tissue to be excitable (Lin et al., 1999).

It is well established that elevated extracellular potassium ion concentration ($[K^+]_o$), which often accompanies such heart disturbances as ischemia (Gettes, 1991) and hyperkalemia (Surawicz, 1995), changes the resting transmembrane potential and alters the excitability of cardiac tissue. In humans normal $[K^+]_o$ is 5.4 mM, and the resting membrane potential is -84 mV. Increasing $[K^+]_o$ to 10 mM elevates the resting membrane potential to approximately -67 mV (Surawicz, 1995). However, at transmembrane potentials above -70 mV the sodium inactivation gates are closed, rendering the tissue unexcitable (Beeler and Reuter, 1977).

We hypothesize that elevated $[K^+]_o$, as might occur during ischemia, not only alters excitation but also affects the mechanism of stimulation. In this article we report epifluorescence data from a series of experiments utilizing diastolic anodal stimulation in which the effect of $[K^+]_o$ elevation was examined. We show that under normal $[K^+]_o$ conditions, the excitation mechanism is anode-make. However, under elevated $[K^+]_o$ conditions the excitation mechanism is revealed as anode-break.

MATERIALS AND METHODS

Experimental preparation and protocol

All experiments were conducted in accordance with National Institutes of Health regulations for the ethical use of animals in research and were approved in advance by the Vanderbilt Institutional Animal Care and Use Committee.

New Zealand white rabbits ($n = 10$) weighing 2–3 kg were first preanesthetized with intramuscular ketamine (50 mg/kg). The animals were then intravenously heparinized (1000 units) and subsequently anesthetized with sodium pentobarbital (50 mg/kg). After a midsternal incision, the hearts were rapidly excised and moved to a Langendorff perfusion system. The

Submitted September 13, 2002, and accepted for publication January 28, 2003.

Address reprint requests to Dr. John P. Wikswo, Dept. of Physics and Astronomy, Vanderbilt University, VU Station B 351807, Nashville, TN 37235-1807. Tel.: 615-343-4124; Fax: 615-322-4977; E-mail: john.wikswo@vanderbilt.edu.

0006-3495/03/05/3470/10 $2.00

ascending aorta was cannulated and secured to perfuse the coronary arteries in a retrograde manner with an oxygenated Tyrode's solution containing (in mM) 130 NaCl, 4 KCl, 2 $CaCl_2$, 1 $MgCl_2$, 1.5 NaH_2PO_4, 23 $NaHCO_3$, and 10 glucose. In each experiment, $[K^+]_o$ was initially 4 mM (normal) and was subsequently raised to 8 mM by adding the appropriate amount of KCl to the existing perfusate solution. After $[K^+]_o$ was raised, a 10-min equilibration time elapsed before subsequent data collection. The perfusate was continuously bubbled with a 95% oxygen/5% carbon dioxide mixture, and the temperature and pH were continuously maintained at 37°C and 7.4 ± 0.05, respectively. Coronary perfusion pressure was regulated to 50 mm Hg. The hearts were exposed to the air during the experiments.

After an equilibration time of 20 min to allow sinus rhythm stabilization, the hearts were stained with 200 μL of di-4-ANEPPS (Molecular Probes, Eugene, OR) stock solution (0.5 mg/mL dimethyl sulfoxide) administered via a bubble trap above the aorta. Diacetyl monoxime (DAM) was added to the Tyrode's solution at a concentration of 15 mM to block muscle contraction and, hence, lessen motion artifacts in the fluorescence data. In all experiments only the anterior left ventricle was imaged.

Electrical stimulation was conducted via both bipolar and unipolar electrodes. The bipolar pacing electrode (S1) was constructed from two platinum wires (0.25-mm diameter) enclosed in glass with only the tips of the wires exposed. The distance between the two tips was 1 mm. The bipolar pacing electrode was placed on the right ventricle close to septum, 8–9 mm from the unipolar testing electrode. The unipolar testing electrode (S2), also made from platinum wire (0.25-mm diameter), was positioned centrally on the anterior left ventricle. The camera field of view was centered around the testing electrode. A small piece of titanium mesh placed against the posterior left ventricle served as the reference testing electrode. The electrical stimuli in the experiments were provided by computer-controlled current sources (Bloom Associates, Narberth, PA). The heart was constantly paced at a 350-ms cycle length with 2-ms electrical stimuli (S1) of strength equal to two times the diastolic stimulation threshold. Anodal test stimuli (S2) of 0.1–10 mA amplitude and 10-ms duration were applied at a S1-S2 coupling interval of 350 ms, unless otherwise stated.

To measure the transmembrane potential directly, 10 additional experiments were conducted using microelectrodes. Action potentials at multiple sites were recorded by using floating 3-M KCl-filled microelectrodes. The microelectrodes were pulled from borosilicate glass capillaries (World Precision Instruments, Sarasota, FL) by a micropipette puller (Model P80/PC, Sutter Instrument, Novato, CA). The microelectrode tips were mounted on 50-μm-diameter platinum wire. The Ag/AgCl reference electrode, 8 mm in diameter and 1 mm in thickness (EP8, World Precision Instruments), was placed in the left ventricular cavity. The electrodes were connected to the input probes of a dual differential electrometer (model FD223, World Precision Instruments). The signals were digitized, visualized, recorded, and analyzed by a digital oscilloscope (Infinium, Hewlett-Packard, Palo Alto, CA). The sampling rate for data acquisition was 10 kHz. All microelectrode measurements were conducted on the anterior left ventricle using the same perfusion setup as for the optical studies.

Optical imaging and data analysis

The fluorescence was excited by a diode-pumped, solid-state laser (Verdi, Coherent, Santa Clara, CA) at a wavelength of 532 nm. The illumination was delivered to the heart with a double-beam illumination scheme (Lin et al., 1999). The emitted light was passed through a cutoff filter (no. 25 Red, 607 nm, Tiffen, Hauppauge, NY) and imaged with a high-speed CCD camera (Model CA D1-0128T, Dalsa, Waterloo, ON, Canada). The faceplate of the camera was cooled via a 15°C refrigerated bath. The data were acquired at 2-ms intervals with 12-bit resolution from 128 × 128 sites simultaneously over a 12 × 12 mm area. The digitized pixel intensity from the digital camera was transferred to a PCI bus-master frame grabber board (IC-PCI, Imaging Technology, Bedford, MA) mounted in an IBM-compatible personal computer (Dell Precision Workstation 610, Dell Computer, Round Rock, TX).

The optical data were first normalized pixel-by-pixel according to fluorescence changes during the last pacing response and then the resulting images were voltage-calibrated according to the microelectrode measurements. The resting membrane potential and action potential amplitude were −85 mV and 112 mV under normal $[K^+]_o$ (4 mM) and −68 mV and 95 mV under elevated $[K^+]_o$ (8 mM), respectively. All data presented in this article have been filtered to improve the signal-to-noise ratio. Data depicting the transmembrane potential distribution were spatially filtered with an 8 × 8 Gaussian filter. These spatially filtered data were used to compute the optical dV/dt_{max} measurements.

We utilized time-space analysis (Pertsov et al., 1993; Gray et al., 1995; Berenfeld et al., 2002) to examine the stimulation mechanism. To explore the evolution of electrical activity during stimulation, time-space plots were constructed for lines along and transverse to the fiber direction. The intersection of these two lines roughly coincided with the position of the testing electrode. To construct the time-space plots, the optical data were preprocessed by applying a 5 × 5 Gaussian spatial filter and a 5-point mean temporal filter two times.

RESULTS

Moderate anodal stimulation of diastolic tissue for normal $[K^+]_o$

Fig. 1 illustrates the tissue response to 6-mA amplitude (3× threshold), 10-ms diastolic anodal stimulation delivered at an S1-S2 coupling interval of 350 ms.

The image of the transmembrane potential distribution during stimulation is shown in Fig. 1 *A*. The experimental data correspond to results previously reported (Knisley, 1995; Neunlist and Tung, 1995; Wikswo, Jr. et al., 1995). The transmembrane potential distribution map exhibits the expected central dog-bone-shaped virtual anode (VA) and a pair of adjacent virtual cathodes (VC). Fig. 1 *B* shows four superimposed optical signals: two at VC (*red*) locations and two at VA (*blue*) locations. The VC action potentials initiate at the beginning of the stimulus. The VA traces reveal initial hyperpolarization, such that the VA action potentials initiate long after the VC action potentials. The peak rate of rise, dV/dt_{max}, is greater for the VA action potentials than for the VC ones. Traces were selected for calculation by random sampling in the VA and VC regions. For eight traces in the VA region dV/dt_{max} is 12.3 ± 0.4 mV/ms, while dV/dt_{max} is 6.0 ± 0.8 mV/ms for eight traces in the VC regions.

The time-space plots for lines longitudinal and transverse to the fiber direction are presented in Fig. 1, *C* and *D*, respectively. These lines are depicted with white and black dashed lines in Fig. 1 *A*. Fig. 1 *C* shows that excitation propagates from two locations that correspond spatially to the virtual cathodes in Fig. 1 *A*. The red arrows in Fig. 1 *C* indicate the two pixel locations (VC1 and VC2) of the VC traces shown in Fig. 1 *B*. Similarly, the blue arrows in Fig. 1 *D* show the position of the two pixels VA1 and VA2.

To compare the activation time of the VC and VA regions, we drew an isochronal line (horizontal) in both Fig. 1 *C* and *D*. One can see that activation first begins in the VC regions. The slope of the line tangent to the depolarization

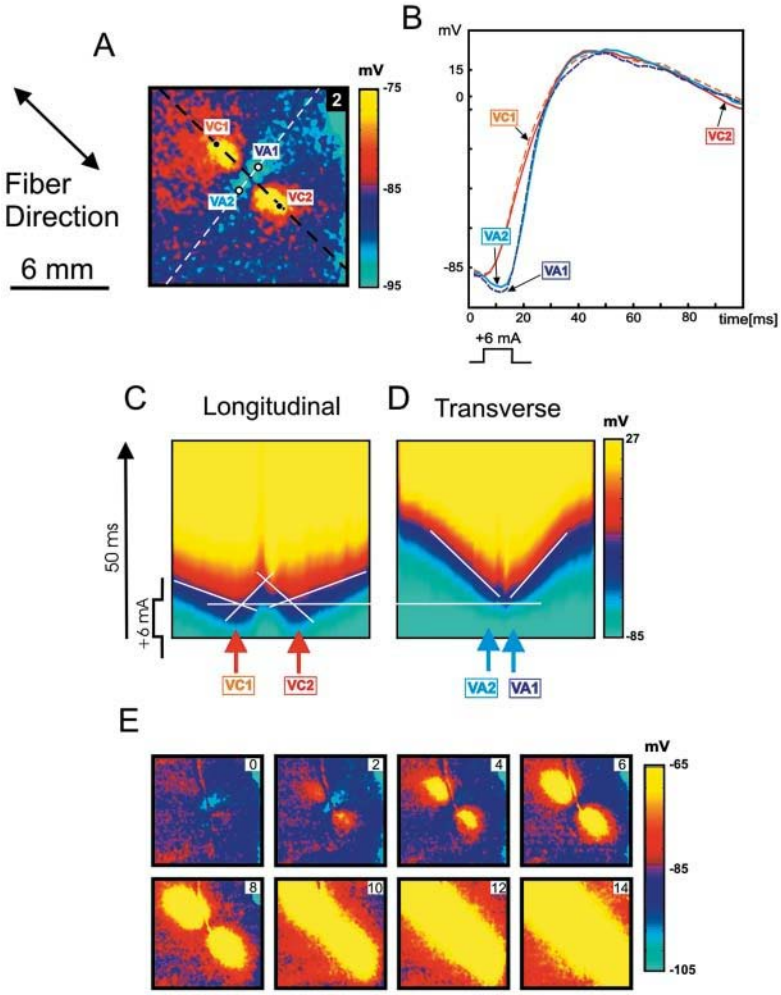

FIGURE 1 Anodal-make response to diastolic 3× threshold stimulation for normal $[K^+]_o$ (4 mM). The anodal S2 stimulus was 6 mA in amplitude, 10 ms in duration, and applied at an S1-S2 coupling interval of 350 ms. (*A*) Image of the transmembrane potential distribution 2 ms after the onset of S2 point stimulation at the center of the image. (*B*) Four representative traces recorded within the virtual cathode (*red*) and virtual anode (*blue*) areas. The pixel locations for these traces are marked with white and black dots in *A*. (*C* and *D*) Time-space plots for lines longitudinal and transverse to the fiber direction (*white* and *black dashed lines* in *A*). The white horizontal isochronal line corresponds to 8 ms after the beginning of S2. The white slanted lines in *C* demonstrate the inward and outward propagation velocity along the fiber direction. The white slanted lines in *D* demonstrate the outward propagation velocity transverse to the fiber direction. The blue and red arrows indicate the location of the pixels depicted by black and white dots in *A*. (*E*) The transmembrane potential distribution as a function of time. The numbers in the upper right represent the time [ms] since the onset of S2.

front (drawn approximately at the −30 mV contour) reveals the conduction velocity along (Fig. 1 *C*) and transverse (Fig. 1 *D*) to the fiber direction. Conduction velocity is inversely related to the slope of the lines drawn in the time-space plots. It is seen that propagation from the VC regions is faster in the outward direction than inward toward the central hyperpolarized VA region (Fig. 1 *C*). Outward conduction velocities indicated by the drawn lines are 65 and 61 cm/s whereas the inward conduction velocities for the drawn lines are 27 and 24 cm/s. As was expected, there is anisotropy in the conduction velocity along and transverse to the fiber direction. Fig. 1 *C* shows faster conduction longitudinal to the fiber direction in comparison with transverse to the fiber direction, as shown in Fig. 1 *D*. The two transverse conduction velocities are 21 and 25 cm/s. Our longitudinal and transverse conduction velocity measurements are in agreement with those computed by Boersma et al. (1991).

Images of the transmembrane potential distribution at 2-ms intervals after the onset of S2 are shown in Fig. 1 *E*. Excitation originates in the two VC regions, indicating anodal-make stimulation.

Threshold anodal stimulation of diastolic tissue for normal $[K^+]_o$

In contrast to the results for moderate anodal stimulation described in Fig. 1, in most experiments we did not observe symmetric activation patterns for threshold anodal stimulation. In the particular experiment described, the threshold anodal stimulus was a 2 mA, 10 ms duration pulse delivered at an S1-S2 coupling interval of 350 ms.

Fig. 2 demonstrates the typical situation in which one of the VC regions reveals more positive polarization than the other. This stronger VC region is the site of excitation initiation. The time traces in Fig. 2 *B* show delay in excitation between the two VC areas. Activation is first observed for VC2, and the resulting wave front initiates activation in the VA region (*blue traces*, VA1 and VA2). VC1 activation occurs last. As was the case in Fig. 1, the peak rate of rise is greater for the VA action potentials than for the VC ones. However, the magnitude of and the difference in dV/dt_{max} for the VA and VC regions are smaller for threshold stimulation. For eight randomly selected traces in the VA region dV/dt_{max} is 6.3 ± 0.5 mV/ms, whereas for eight

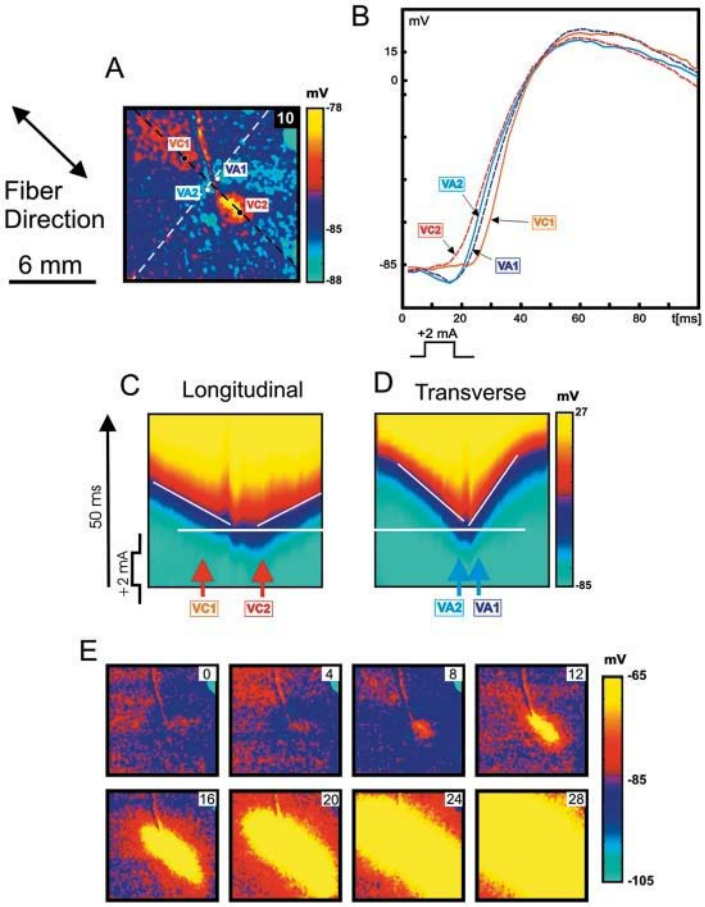

FIGURE 2 Anodal-make response to diastolic threshold stimulation for normal $[K^+]_o$ (4 mM). The anodal S2 stimulus was 2 mA in amplitude, 10 ms in duration, and applied at an S1-S2 coupling interval of 350 ms. (*A*) Image of the transmembrane potential distribution 10 ms after the onset of S2 point stimulation at the center of the image. (*B*) Four representative traces recorded within the virtual cathode (*red*) and virtual anode (*blue*) areas. The pixel locations for these traces are marked with white and black dots in *A*. (*C* and *D*) Time-space plots for lines longitudinal and transverse to the fiber direction (*white* and *black dashed lines* in *A*). The white horizontal isochronal line corresponds to 16 ms after the beginning of S2. The white slanted lines demonstrate propagation velocity along (*C*) and transverse (*D*) to the fiber direction. The blue and red arrows indicate the location of the pixels depicted by black and white dots in *A*. (*E*) The transmembrane potential distribution as a function of time. The numbers in the upper right represent the time [ms] since the onset of S2.

randomly selected traces in the VC regions, dV/dt_{max} is 4.8 ± 0.4 mV/ms.

Fig. 2, *C* and *D* show time-space plots for lines along and transverse to the fiber direction. Lines tangent to the depolarization front are drawn (at approximately the −30 mV contour) to show the conduction velocities. Activation is first observed in the VC2 area (Fig. 2 *C*), followed by activation in the VA regions (Fig. 2 *D*). Activation in the VC1 area is delayed (Fig. 2 *C*). These time-space plots again reveal the expected anisotropic conduction velocity along (43 and 46 cm/s) and transverse (27 and 17 cm/s) to the fiber direction. Note the marked decrease in longitudinal conduction velocity for threshold stimulation in comparison with moderate stimulation (Fig. 1 *C*). Both the time-space plot in the longitudinal direction (Fig. 2 *C*) and the succession of the transmembrane potential images (Fig. 2 *E*) also demonstrate asymmetric anodal-make excitation for threshold anodal stimulation.

Long duration, strong anodal stimulation of refractory tissue for normal $[K^+]_o$

To obtain an episode of anodal-break stimulation, a 20-mA amplitude (10× threshold), 150-ms anodal S2 stimulus was delivered to refractory tissue using an S1-S2 interval of 80 ms.

Fig. 3 *A* demonstrates the stimulation timing (*black arrows* at the *bottom*) and tissue response to S1 and S2 stimulation. The red trace corresponds to the virtual cathode pixel location VC1 while the blue trace corresponds to the virtual anode pixel location VA2, as depicted in Fig. 3 *B*, showing the transmembrane potential distribution 82 ms after the onset of S2. The expected dog-bone-shaped virtual anode and pair of adjacent virtual cathodes are shown.

The virtual cathode and virtual anode optical traces are presented in Fig. 3 *C*. The beginning of the timescale corresponds to the 130th ms of the S2 pulse (20 ms before the stimulus termination). During S2 stimulation, the voltage difference between the virtual anodes and virtual cathodes is ~40 mV. Immediately after S2 termination (*second dotted black line* in Fig. 3 *A*), the voltage in the virtual cathode areas decreases (*red traces*), whereas the virtual anode voltage (*blue traces*) increases, indicating charge diffusion from the virtual cathodes to the virtual anode area. After the VC and VA traces intersect, the voltages in the virtual anode region are greater than those in the virtual cathode regions, suggesting the initiation of excitation in the virtual anode region. Fig. 3 *F* shows images of transmembrane potential distribution as a function of time. The frame labeled 16 ms approximately corresponds to the time at which the VC and

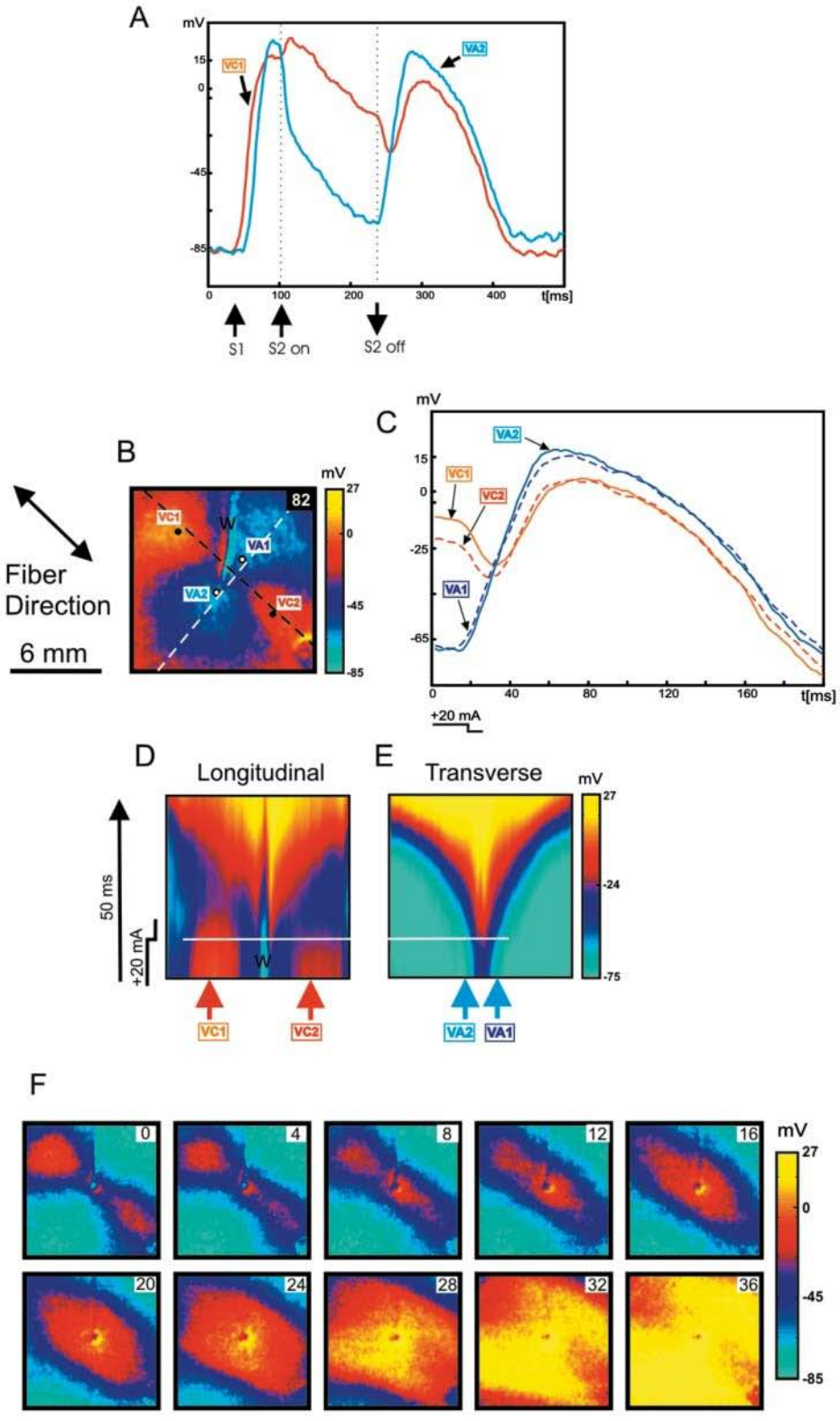

FIGURE 3 Anodal-break response to strong systolic stimulation for normal $[K^+]_o$ (4 mM). The anodal S2 stimulus was 20 mA in amplitude, 150 ms in duration, and applied at an S1-S2 coupling interval of 80 ms. (*A*) Representative traces recorded within the virtual cathode (*red*) and virtual anode (*blue*) area depicting the response to S1 and S2 stimulation. The black arrows underneath the plot show the stimulus timing. (*B*) Image of the transmembrane potential distribution 82 ms after the onset of S2 point stimulation at the center of the image. The pixel locations for the traces in *A* and *C* are indicated by the white and black dots. (*C*) Four representative traces recorded within the virtual cathode (*red*) and virtual anode (*blue*) areas depicting the response at the end of S2 and after S2 termination. (*D* and *E*) Time-space plots for lines longitudinal and transverse to the fiber direction (*white and black dashed lines* in *B*). The white horizontal isochronal line corresponds to the termination of S2. The white slanted lines demonstrate propagation velocity along (*D*) and transverse (*E*) to the fiber direction. The blue and red arrows indicate the location of the pixels depicted by black and white dots in *B*. Data artifacts caused by the testing electrode lie underneath the black W's in the images of *B* and *D*. (*F*) The transmembrane potential distribution as a function of time. The numbers in the upper right represent the time [ms] since the termination of S2.

VA traces intersect in Fig. 3 *C*. Note that the final activation pattern in the series, at 36 ms, shows dog-bone-shaped activation, consistent with a dog-bone-shaped virtual anode and anodal-break excitation.

The virtual cathodes are revealed in the longitudinal time-space plot (Fig. 3 *D*) as red areas (indicated with *red arrows*) during stimulation. The color change of the virtual cathode regions from red to blue after the stimulus is turned off

reflects the diffusion of positive charge into the more negative virtual anode area, as was discussed for Fig. 3 *C*. The isochronal lines (horizontal white lines) reveal that activation in the virtual anode occurs earlier (Fig. 3 *E*) than in the virtual cathodes (Fig. 3 *D*), again indicating anodal-break stimulation. Conduction velocities were not computed for Fig. 3, *D* and *E*, because there are no stationary velocities to measure.

Threshold anodal stimulation of diastolic tissue for elevated $[K^+]_o$

Fig. 4 illustrates the tissue response to anodal threshold stimulation during diastole for 8 mM $[K^+]_o$ conditions.

Fig. 4 *A* shows the transmembrane potential distribution during a 6-mA (threshold), 10-ms anodal S2 stimulus using an S1-S2 interval of 350 ms for elevated $[K^+]_o$. The polarization pattern is very similar to that produced with the exact same stimulation parameters for normal $[K^+]_o$ (Fig. 1 *A*). A hyperpolarized region lies around the point of stimulation, and a pair of adjacent depolarized regions is oriented along the fiber direction.

Four representative traces from the virtual cathodes (*red*) and virtual anode (*blue*) region are depicted in Fig. 4 *B*. The optical signals initially reveal depolarization in the VC areas and hyperpolarization in the VA area. Moreover, although the VC regions are distal from the S2 electrode location, the magnitude of the VC depolarization is significantly larger than the magnitude of the hyperpolarization in the VA region, which surrounds the S2 electrode site. After S2 termination, the VC traces reveal slight negative polarization whereas the VA traces exhibit depolarization. After the VC and VA traces intersect, the VA optical signals show activation before the VC signals. This behavior is similar to that shown for stimulation of refractory tissue in normal $[K^+]_o$ (Fig. 3 *C*), suggesting excitation initiation in the VA region. Because of the biphasic nature of the VC time traces, dV/dt_{max} was not measured for the virtual electrode regions for the elevated $[K^+]_o$ situation.

Time-space plots for lines longitudinal and transverse to the fiber direction are presented in Fig. 4, *C* and *D*. In Fig. 4 *C* the slope of the tangent line of the depolarization edge (drawn approximately at the −55 mV contour) reveals no longitudinal wave front propagation away from the S2 electrode site for 25 ms after S2 termination. However, the time-space plot in Fig. 4 *D* shows very slow transverse propagation (6 and 5 cm/s) out of the virtual anode during this time period.

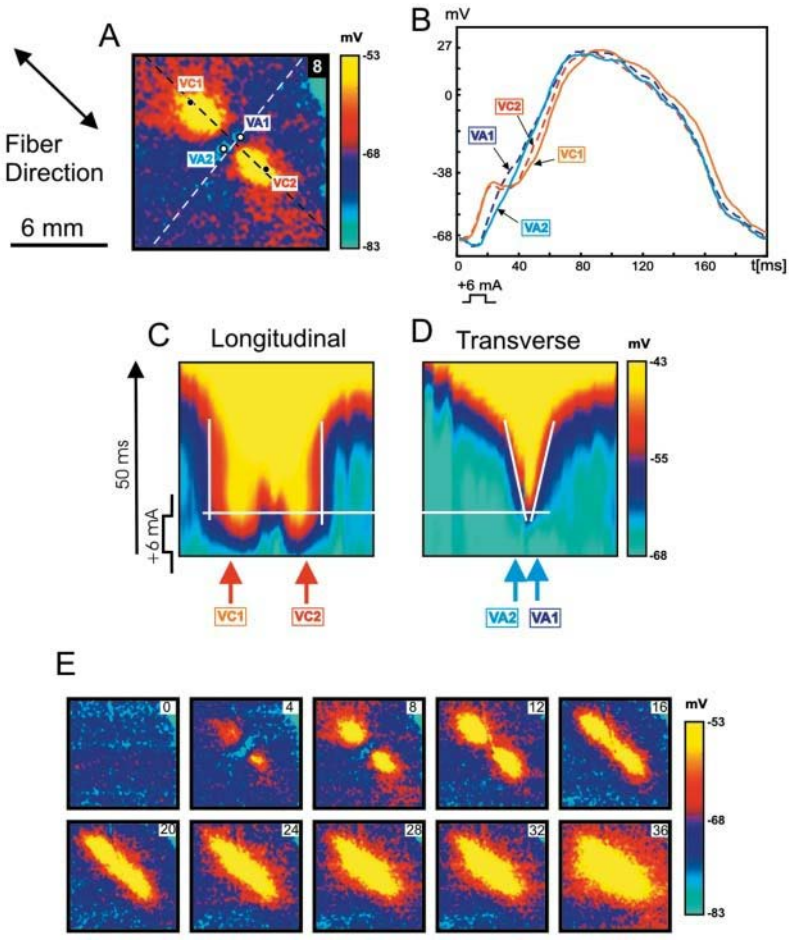

FIGURE 4 Anodal-break response to diastolic threshold stimulation for elevated $[K^+]_o$ (8 mM). The anodal S2 stimulus was 6 mA in amplitude, 10 ms in duration, and applied at an S1-S2 coupling interval of 350 ms. (*A*) Image of the transmembrane potential distribution 8 ms after the onset of S2 point stimulation at the center of the image. (*B*) Four representative traces recorded within the virtual cathode (*red*) and virtual anode (*blue*) areas. The pixel locations for these traces are marked with white and black dots in *A*. (*C* and *D*) Time-space plots for lines longitudinal and transverse to the fiber direction (*white* and *black dashed lines* in *A*). The white horizontal isochronal line corresponds to the termination of S2. The white slanted lines demonstrate propagation velocity along (*C*) and transverse (*D*) to the fiber direction. The blue and red arrows indicate the location of the pixels depicted by black and white dots in *A*. (*E*) The transmembrane potential distribution as a function of time. The numbers in the upper right represent the time [ms] since the onset of S2.

Images of the transmembrane potential distribution as a function of time are presented in Fig. 4 *E*. The stimulus was turned on in frame 0 and was terminated 10 ms later, between the frames depicting 8 and 12 ms. Although the tissue is diastolic, S2 fails to initiate excitation in the VC areas. Instead, after the cessation of S2 (12 ms frame), the charge in the VC areas begins to diffuse into the hyperpolarized VA region located between the VC areas (16–36-ms frames), and excitation is initiated in the VA (16-ms frame).

It should be noted that the longitudinal axis of the spreading excitation wave (Fig. 5 *A*, *blue line*) forms an approximate 35° angle with the VC location axis (Fig. 5 *A*, *green line*), which was assumed to coincide with the fiber direction. However, for normal $[K^+]_o$ (4 mM), the main ellipse axis of the propagating wave front concurred with the VC location axis (Fig. 5 *B*, *green line*). The data depicted for both the elevated $[K^+]_o$ (Fig. 5 *A*) and normal $[K^+]_o$ (Fig. 5 *B*) situations are the same data described in Figs. 4 and 1, respectively. In both cases the anodal S2 was a 6-mA, 10-ms pulse delivered at an S1-S2 interval of 350 ms.

Fig. 5 also demonstrates time-space plots for the VC location axis (Fig. 5 *C*) and the main axis of the spreading excitation wave (Fig. 5 *D*) for the elevated $[K^+]_o$ situation (Fig. 5 *A*). Fig. 5 *D* shows excitation propagation after stimulus cessation, but no propagation is observed along the VC axis during the same time period (Fig. 5 *C*). It should also be mentioned that slope of the tangent lines in Fig. 5 *D* reveals faster conduction velocity (9 cm/s) in comparison with those in Fig. 4 *D* for transverse to the fiber direction.

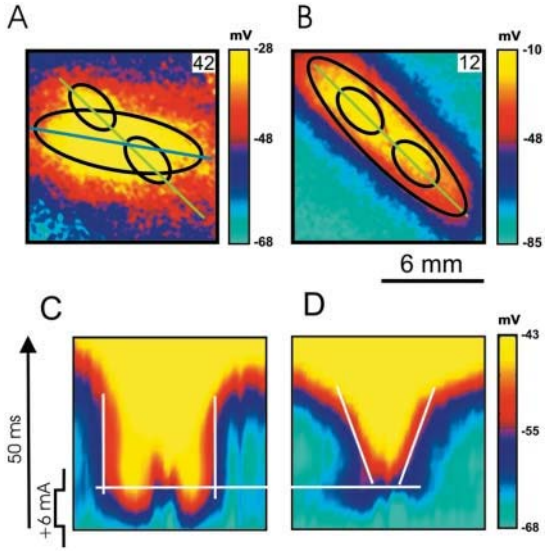

FIGURE 5 Wave front and virtual cathode location for normal (4 mM) and elevated (8 mM) $[K^+]_o$. Images of the transmembrane potential distribution for (*A*) elevated and (*B*) normal $[K^+]_o$. The smaller ellipses depict the virtual cathode locations, and the large ellipses describe the propagating wave fronts. (*C* and *D*) The time-space plots constructed along the (*C*) green and (*D*) blue lines in *A*. The white horizontal isochronal line corresponds to the termination of S2. The white slanted lines show propagation velocity along the axes in *A*.

Effect of elevated $[K^+]_o$ on the transmembrane potential

Fig. 6 illustrates the effects of elevated $[K^+]_o$ on the transmembrane potential. Elevation of $[K^+]_o$ from 4 mM (Fig. 6 *A*) to 8 mM (Fig. 6 *B*) raises the resting membrane potential from -84.8 ± 2.3 mV (75 measurements from 37 cells of eight hearts) to -67.5 ± 2.3 mV (66 measurements from 27 cells of seven hearts) and reduces the action potential amplitude from 112.0 ± 4.0 mV (74 measurements from 36 cells of nine hearts) to 95.5 ± 2.7 mV (68 measurements from 28 cells of seven hearts).

DISCUSSION

Cathodal and anodal make-and-break stimulation was first demonstrated by Dekker in 1970 (Dekker, 1970). The cellular mechanisms of these four modes for stimulating cardiac tissue remained a mystery until Roth's 1995 modeling analysis (Roth, 1995) demonstrated the role played by the differences between the anisotropies of the intracellular and extracellular spaces in the response of the cardiac bidomain to point stimulation. The subsequent measurements by Wikswo et al. (1995) provided clear evidence that the response to suprathreshold point stimulation in the isolated rabbit heart was consistent with the explanation of the four modes provided by Roth.

Nikolski et al. (2002) report ''paradoxical results'' for threshold stimulation of cardiac tissue. In this article, we demonstrate that the identification of the mode of stimulation for threshold stimulation is difficult, in part because the VC and VA areas are smaller and less pronounced and hence less easily delineated, because charge diffusion does not necessarily lead to a rapid response of the tissue, and because heterogeneities in the tissue excitability can lead to asymmetries in the threshold stimulus response. Recognizing the possible difficulty in interpreting optical recordings of excitation patterns for threshold stimuli, we have developed a series of visualization techniques and criteria that allow us to discriminate between anodal and cathodal make-and-break excitation. The examples we show in Figs. 1–4 were chosen to

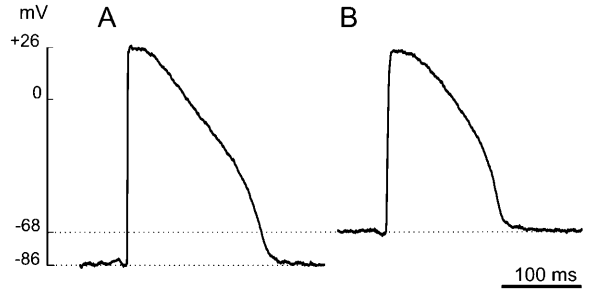

FIGURE 6 Microelectrode measurements of transmembrane potential for normal (4 mM) and elevated (8 mM) $[K^+]_o$. Typical action potentials recorded using microelectrodes for (*A*) normal and (*B*) elevated $[K^+]_o$.

provide a pedagogically rigorous explanation of these techniques and criteria.

Furthermore, to provide a means to adjust the response of the tissue to the stimulation while keeping the stimulus parameters constant, we have conducted a series of experiments using elevated extracellular potassium, which raises the transmembrane potential and in turn increases the sodium channel inactivation. Partial inactivation of the sodium channels is known to increase the threshold and to slow the rise of the action potential (Katz, 1992). The traces presented in Fig. 4 *B* resulting from anodal stimulation in high $[K^+]_o$ clearly show significant deceleration of the optical action potential upstrokes in comparison to those for normal $[K^+]_o$ in Fig. 1 *B*. Under 4 mM $[K^+]_o$, dV/dt_{max} for 10 randomly selected traces is 8.7 ± 0.5 mV/ms, whereas under 8 mM $[K^+]_o$ dV/dt_{max} decreases to 5.2 ± 0.4 mV/ms. For the microelectrode measurements dV/dt_{max} is 174.8 ± 30 mV/ms (mean ± SD, $n = 22$) and 40.3 ± 5.4 mV/ms (mean ± SD, $n = 26$) for normal and elevated $[K^+]_o$, respectively. This deceleration of action potential upstroke is a consequence of the depolarizing effect of elevated $[K^+]_o$ on the resting membrane potential and also may be the result of a voltage-independent effect on the inwardly rectifying K^+ current (Whalley et al., 1994; Nygren and Giles, 2000). The discrepancy between the microelectrode and optical dV/dt_{max} measurements is due to the high sampling rate of the microelectrode data and fluorescence averaging within a volume of tissue in the optical data (Girouard et al., 1996a).

The traces in Fig. 4 *B* also demonstrate that for a 6-mA stimulus, because of the slowed upstroke caused by elevated $[K^+]_o$, the VC regions cannot sufficiently depolarize to reach threshold during the 10-ms stimulus duration. The hyperpolarization in the VA area appears faster that the VC depolarization, but is a much weaker response. Under the condition of the partially elevated resting membrane potential, the hyperpolarization opens voltage-dependent sodium channel inactivation gates and causes increased excitability in the VA region. Thus, although the depolarization in the VC areas is too weak to overcome threshold and initiate an action potential, there is sufficient charge accumulation in the VC areas to stimulate the VA region after S2 termination, resulting in anodal-break stimulation.

In a recent study of acute global ischemia (Cheng et al., 2002), the authors found that ischemia significantly changed repolarization characteristics but only slightly decreased conduction. This is in sharp contrast with our findings of obvious slowed conduction during elevated $[K^+]_o$. The Cheng et al. ischemic model is created by decreasing perfusion flow rate to 25% of normal. In this decreased flow state, we believe there may still be enough flow to allow extracellular potassium to wash out. Therefore $[K^+]_o$ may not have been significantly elevated in their study, explaining why they do not see decelerated action potential upstrokes.

The elevation of $[K^+]_o$ has biphasic effect on excitability. As was shown in pigs, the ventricular threshold of excitability decreases when the plasma $[K^+]_o$ is moderately elevated, but increases sharply when plasma $[K^+]_o$ exceeds 7–9 mM (Gettes and Surawicz, 1968). For intermediate concentrations of $[K^+]_o$ (6–7 mM) we observed make-excitation for 10-ms threshold stimulation (data not shown), as was the case for the normal 4 mM $[K^+]_o$ situation. Therefore, in our rabbit experiments we analyzed the mechanism of diastolic stimulation in the $[K^+]_o$ range of 8–9 mM. We observed anodal-break stimulation for 8 mM $[K^+]_o$ in 7 of the 10 experiments. In these cases elevation of $[K^+]_o$ from 4 mM to 8 mM increased the anodal threshold from 1.53 ± 0.5 mA (mean ± SD, $n = 7$) to 3.41 ± 1.3 mA (mean ± SD, $n = 7$) (two-tailed, paired Student's *t*-test, $P < 0.01$). In the remaining three experiments, to observe anodal-break stimulation $[K^+]_o$ had to be increased to 9 mM. For these hearts, elevation of $[K^+]_o$ from 4 mM to 9 mM increased the anodal threshold from 1.33 ± 0.7 mA (mean ± SD, $n = 3$) to 2.77 ± 0.9 mA (mean ± SD, $n = 3$) (two-tailed, paired Student's *t*-test, $P < 0.05$). Subsequent elevation of $[K^+]_o$ above 9 mM significantly decreases the signal-to-noise ratio. When $[K^+]_o$ was raised to 12 mM, tissue excitability was completely depressed, and stimuli as large as 10 mA elicited no response.

According to anatomical architecture, myocardium is characterized by fiber axis rotation. This rotation is counterclockwise from the epicardial to endocardial surface with a rotation angle of ~120° (Streeter et al., 1969; Streeter, 1979). Additionally, optical recordings from the heart surface are actually weighted averages of fluorescence from a tissue depth that has been estimated to be 300–500 μm (Knisley, 1995; Girouard et al., 1996a) all the way up to 1–2 mm (Efimov et al., 1999; Al-Khadra et al., 2000; Baxter et al., 2001; Ding et al., 2001). In our experiments with elevated $[K^+]_o$, the anodal-break stimulated propagating wave front forms an ellipse with axes that do not coincide with the axes longitudinal and transverse to the fiber direction (Fig. 5 *A*). This apparent discrepancy may be explained by wave front propagation in deeper myocardial layers.

Though beyond the scope of this article, it may be worthwhile to conduct detailed studies of the ionic mechanisms that are involved in the conversion of the stimulation mechanism during elevated $[K^+]_o$. Such experimental studies may include the addition of pharmacological sodium channel blockers and the use of another excitation-contraction decoupler, such as cytochalasin D. However, little modeling work exists to study the effects of elevated $[K^+]_o$. Detailed studies of the involved ionic mechanisms would be best and most easily conducted by mathematical modeling due to the complexity of such experimental undertakings.

Because $[K^+]_o$ elevation accompanies ischemia, our data suggest break-stimulation as a likely mechanism for threshold unipolar anodal stimulation not only during hyperkalemia but also during ischemic events. Given the increased recognition of the role of break-excitation in cardiac defibrillation (Skouibine et al., 1999), and the presence of increased extracellular potassium during fibrillation, it may be

worthwhile to examine in greater detail the role of elevated $[K^+]_o$ in the defibrillation process.

Limitations of the study

As described earlier, optical signals originate not only from surface epicardial layers but also from layers deeper beneath the surface. The resulting three-dimensional data and the three-dimensional myocardial structure make the image patterns more difficult to interpret. Cryoablation of the endocardium to obtain a preparation in which only a thin epicardial layer is viable would help to alleviate this problem (Allessie et al., 1989; Brugada et al., 1990, 1991; Schalij et al., 1992; Knisley and Hill, 1995; Girouard et al., 1996b; Baxter et al., 2001).

Current optical imaging techniques require the use of an excitation-contraction decoupler, such as DAM, to eliminate motion artifacts in data collection. DAM is known to change several membrane conductances, causing some electrophysiological effects including decreased action potential duration (Liu et al., 1993), decreased dV/dt_{max} (Li et al., 1985), and decreased conduction velocity (Knisley and Hill, 1995). While the use of DAM may quantitatively affect our results, comparison of data in normal and high $[K^+]_o$ situations is valid because DAM was used in all experiments.

When we elevated $[K^+]_o$, we did not alter other ion concentrations in the perfusate to maintain the same osmolarity as the original 4 mM $[K^+]_o$ perfusate. The high $[K^+]_o$ perfusate, therefore, has a higher osmolarity than the normal $[K^+]_o$ perfusate. However, a change in $[K^+]_o$ from 4 mM to 8 mM increases the osmolarity by only 8 mOsm/L, or a total change of 2.4%. Such a small change should have minimal effect upon the myocardial cells.

We thank Mark-Anthony P. Bray, Jonathan M. Gilligan, and Bradley J. Roth for their encouragement and numerous suggestions.

This work was supported by the National Institutes of Health (R01-HL58241-05 and 5T32-HL07411), the American Heart Association (0215128B), and the Academic Venture Capital Fund of Vanderbilt University.

REFERENCES

Al-Khadra, A., V. Nikolski, and I. R. Efimov. 2000. The role of electroporation in defibrillation. *Circ. Res.* 87:797–804.

Allessie, M. A., M. J. Schalij, C. J. Kirchhof, L. Boersma, M. Huybers, and J. Hollen. 1989. Experimental electrophysiology and arrhythmogenicity. Anisotropy and ventricular tachycardia. *Eur. Heart J.* (10)E:2–8. (Suppl.).

Baxter, W. T., S. F. Mironov, A. V. Zaitsev, J. Jalife, and A. M. Pertsov. 2001. Visualizing excitation waves inside cardiac muscle using transillumination. *Biophys. J.* 80:516–530.

Beeler, G. W., and H. Reuter. 1977. Reconstruction of the action potential of ventricular myocardial fibres. *J. Physiol. (Lond.).* 268:177–210.

Berenfeld, O., A. V. Zaitsev, S. F. Mironov, A. M. Pertsov, and J. Jalife. 2002. Frequency-dependent breakdown of wave propagation into fibrillatory conduction across the pectinate muscle network in the isolated sheep right atrium. *Circ. Res.* 90:1173–1180.

Boersma, L., J. Brugada, C. J. Kirchhof, and M. A. Allessie. 1991. The effects of potassium on anisotropic conduction. *In* Cardiac Electrophysiology, Circulation, and Transport. S. Sideman, R. Beyar, and A.G. Kleber, editors. Kluwer Academic Publishers, Boston, MA. pp. 101–108.

Brugada, J., L. Boersma, C. J. Kirchhof, P. Brugada, M. Havenith, H. J. Wellens, and M. Allessie. 1990. Double-wave reentry as a mechanism of acceleration of ventricular tachycardia. *Circulation.* 81:1633–1643.

Brugada, J., L. Boersma, C. J. Kirchhof, V. V. Heynen, and M. A. Allessie. 1991. Reentrant excitation around a fixed obstacle in uniform anisotropic ventricular myocardium. *Circulation.* 84:1296–1306.

Cheng, Y., K. A. Mowrey, V. Nikolski, P. J. Tchou, and I. R. Efimov. 2002. Mechanisms of shock-induced arrhythmogenesis during acute global ischemia. *Am. J. Physiol. Heart Circ. Physiol.* 282:H2141–H2151.

Dekker, E. 1970. Direct current make and break thresholds for pacemaker electrodes on the canine ventricle. *Circ. Res.* 27:811–823.

Ding, L., R. Splinter, and S. B. Knisley. 2001. Quantifying spatial localization of optical mapping using Monte Carlo simulations. *IEEE Trans. Biomed. Eng.* 48:1098–1107.

Efimov, I. R., V. Sidorov, Y. Cheng, and B. Wollenzier. 1999. Evidence of three-dimensional scroll waves with ribbon-shaped filament as a mechanism of ventricular tachycardia in the isolated rabbit heart. *J. Cardiovasc. Electrophysiol.* 10:1452–1462.

Gettes, L., and B. Surawicz. 1968. Effects of low and high concentrations of potassium on the simultaneously recorded Purkinje and ventricular action potentials of the perfused pig moderator band. *Circ. Res.* 23:717–729.

Gettes, L. S. 1991. The electrophysiology of acute ischemia. *In* Cardiac Electrophysiology and Arrhythmias. C. Fisch and B. Surawicz, editors. Elsevier, New York. pp. 13–24.

Girouard, S. D., K. R. Laurita, and D. S. Rosenbaum. 1996a. Unique properties of cardiac action potentials recorded with voltage-sensitive dyes. *J. Cardiovasc. Electrophysiol.* 7:1024–1038.

Girouard, S. D., J. M. Pastore, K. R. Laurita, K. W. Gregory, and D. S. Rosenbaum. 1996b. Optical mapping in a new guinea pig model of ventricular tachycardia reveals mechanisms for multiple wavelengths in a single reentrant circuit. *Circulation.* 93:603–613.

Gray, R. A., J. Jalife, A. Panfilov, W. T. Baxter, C. Cabo, J. M. Davidenko, and A. M. Pertsov. 1995. Nonstationary vortexlike reentrant activity as a mechanism of polymorphic ventricular tachycardia in the isolated rabbit heart. *Circulation.* 91:2454–2469.

Katz, A. M. 1992. The cardiac action potential. *In* Physiology of the Heart. Raven Press, New York. pp. 438–73.

Knisley, S. B. 1995. Transmembrane voltage changes during unipolar stimulation of rabbit ventricle. *Circ. Res.* 77:1229–1239.

Knisley, S. B., and B. C. Hill. 1995. Effects of bipolar point and line stimulation in anisotropic rabbit epicardium: assessment of the critical radius of curvature for longitudinal block. *IEEE Trans. Biomed. Eng.* 42:957–966.

Li, T., N. Sperelakis, R. E. Teneick, and R. J. Solaro. 1985. Effects of diacetyl monoxime on cardiac excitation-contraction coupling. *J. Pharmacol. Exp. Ther.* 232:688–695.

Lin, S.-F., B. J. Roth, and J. P. Wikswo, Jr. 1999. Quatrefoil reentry in myocardium: an optical imaging study of the induction mechanism. *J. Cardiovasc. Electrophysiol.* 10:574–586.

Liu, Y., C. Cabo, R. Salomonsz, M. Delmar, J. Davidenko, and J. Jalife. 1993. Effects of diacetyl monoxime on the electrical properties of sheep and guinea pig ventricular muscle. *Cardiovasc. Res.* 27:1991–1997.

Neunlist, M., and L. Tung. 1995. Spatial distribution of cardiac transmembrane potentials around an extracellular electrode: dependence on fiber orientation. *Biophys. J.* 68:2310–2322.

Nikolski, V. P., A. T. Sambelashvili, and I. R. Efimov. 2002. Mechanisms of make and break excitation revisited: paradoxical break excitation during diastolic stimulation. *Am. J. Physiol. Heart Circ. Physiol.* 282: H565–H575.

Nygren, A., and W. R. Giles. 2000. Mathematical simulation of slowing of cardiac conduction velocity by elevated extracellular $[K^+]$ in a human atrial strand. *Ann. Biomed. Eng.* 28:951–957.

Pertsov, A., M. Vinson, and S. C. Muller. 1993. Three-dimensional reconstruction of organizing centers in excitable chemical media. *Physica D*. 63:233–240.

Roth, B. J. 1995. A mathematical model of make and break electrical stimulation of cardiac tissue by a unipolar anode or cathode. *IEEE Trans. Biomed. Eng*. 42:1174–1184.

Roth, B. J. 1996. Strength-interval curves for cardiac tissue predicted using the bidomain model. *J. Cardiovasc. Electrophysiol*. 7:722–737.

Schalij, M. J., W. J. Lammers, P. L. Rensma, and M. A. Allessie. 1992. Anisotropic conduction and reentry in perfused epicardium of rabbit left ventricle. *Am. J. Physiol.* 263:H1466–H1478.

Sepulveda, N. G., B. J. Roth, and J. P. Wikswo, Jr. 1989. Current injection into a two-dimensional anisotropic bidomain. *Biophys. J*. 55:987–999.

Sepulveda, N. G., and J. P. Wikswo, Jr. 1987. Electric and magnetic fields from two-dimensional anisotropic bisyncytia. *Biophys. J*. 51: 557–568.

Skouibine, K. B., N. A. Trayanova, and P. K. Moore. 1999. Anode/cathode make and break phenomena in a model of defibrillation. *IEEE Trans. Biomed. Eng*. 46:769–777.

Streeter, D. D. 1979. Gross morphology and fiber geometry of the heart. *In* Handbook of Physiology. R. M. Berne, N. Sperelakis, and S. R. Geiger, editors. American Physiological Society, Bethesda, MD. pp. 61–112.

Streeter, D. D., H. M. Spotnitz, D. P. Patel, J. Ross, Jr., and E. H. Sonnenblick. 1969. Fiber orientation in the canine left ventricle during diastole and systole. *Circ. Res*. 24:339–347.

Surawicz, B. 1995. The interrelationship of electrolyte abnormalities and arrhythmias. *In* Cardiac Arrhythmias: Their Mechanisms, Diagnosis, and Management. W. J. Mandel, editor. J.B. Lippincott Company, Philadelphia, PA. 89–109.

Whalley, D. W., D. J. Wendt, C. F. Starmer, Y. Rudy, and A. O. Grant. 1994. Voltage-independent effects of extracellular K^+ on the Na^+ current and phase 0 of the action potential in isolated cardiac myocytes. *Circ. Res*. 75:491–502.

Wikswo, J. P., Jr. 1994. The complexities of cardiac cables: virtual electrode effects. *Biophys. J*. 66:551–553.

Wikswo, J. P., Jr., S.-F. Lin, and R. A. Abbas. 1995. Virtual electrodes in cardiac tissue: a common mechanism for anodal and cathodal stimulation. *Biophys. J*. 69:2195–2210.